Influence of local microstructural variations on the bendability of aluminium extrusions: experiments and crystal plasticity analyses

Bjørn Håkon Frodal[a,b,*], Lars Lodgaard[c], Yngve Langsrud[c], Tore Børvik[a,b], Odd Sture Hopperstad[a,b]

[a]SIMLab – Structural Impact Laboratory, Department of Structural Engineering, NTNU – Norwegian University of Science and Technology, Trondheim, Norway
[b]CASA – Centre for Advanced Structural Analysis, NTNU, Trondheim, Norway
[c]Benteler Automotive Raufoss AS, Raufoss, Norway

Abstract

The bendability of extruded profiles of an age hardenable aluminium alloy is investigated using mechanical tests on flat tensile specimens and bending specimens. Two profile geometries are considered, where the profiles exhibit different grain structure. The microstructure of the profiles in terms of the crystallographic texture and constituent particles is otherwise comparable. While the tensile properties are not that different for the two profiles, their bendability is strongly dependent on the grain structure and is about twice as high for one profile than for the other. A newly proposed coupled damage and single crystal plasticity model is used in finite element analyses of the mechanical tests to investigate the influence of the grain structure on the bending behaviour, and the numerical results are compared to the experimental tests. The crystallographic texture and the grain morphology of the profiles, found by the electron back-scatter diffraction technique, are explicitly represented in the finite element models. The crystal plasticity simulations capture the difference in the bendability of the two profiles, and in agreement with the experiments predict a considerably higher bendability for one of the profiles. It is found that the grain structure affects the shear band formation in these profiles, but also the local texture where the shear bands are located is important for crack initiation and propagation as grains with certain crystallographic orientations may have a higher fracture resistance.

Keywords: Bending, Ductile fracture, Crystal plasticity, Finite element method, Aluminium alloy

1. Introduction

Age hardenable aluminium alloys are widely used in car body panels, aeroplane fuselages, and in load-bearing components for structural applications. High strength and ductility are typically desired for structural applications, and aluminium alloys are attractive due to their high load-bearing capacity and low weight. In addition, properties such as good formability and corrosion resistance, combined with a great potential for recycling, make them appealing to the automotive industry. Lighter materials contribute to producing vehicles with reduced fuel consumption and long-range electrical cars. To uphold strict safety requirements, a combination of high strength and ductility is needed. A material's energy absorbing qualities during impact are essential in, e.g., bumper systems and battery protection units. In these situations, the bendability of a material is often crucial as the protective structures are typically subjected to crushing and bending loads during impact. A material with high bendability is also critical in forming operations used during fabrication of, e.g., body panels.

The thermo-mechanical processing of age hardenable aluminium alloys influences microstructural characteristics such as the grain structure, crystallographic texture and precipitate structure. Thus, by changing

---

Nomenclature

Symbols

A_p	Measured constituent particles area
D_p	Equivalent particle diameter
f_p	Measured area fraction of constituent particles
F	Measured force
$\bar{F}$	Bending force per cross-section area
A_0	Initial cross-section area
ΔL	Displacement of the extensometer
L_0	Initial length of the extensometer
u	Indenter displacement
D	Diameter of the bending test support rollers
a	Gap between the bending test support rollers
h	Thickness of the bending specimen
w	Width of the bending specimen
σ_{eng}	Engineering stress
$\boldsymbol{\sigma}$	Cauchy stress tensor
$\hat{\boldsymbol{\sigma}}$	Co-rotated stress tensor
$\tilde{\boldsymbol{\sigma}}$	Effective stress tensor
$\mathfrak{R}$	Orthogonal rotation tensor
$\mathbf{D}$	Rate-of-deformation tensor
$\hat{\mathbf{D}}$	Co-rotated rate-of-deformation tensor
$\mathbf{D}^e$	Elastic part of $\mathbf{D}$
$\mathbf{D}^p$	Plastic part of $\mathbf{D}$
$\mathbf{W}$	Spin tensor
$\mathbf{W}^e$	Elastic/lattice part of $\mathbf{W}$
$\mathbf{W}^p$	Plastic part of $\mathbf{W}$
$\mathbb{C}$	Fourth order elasticity tensor

$\hat{c}_{11}, \hat{c}_{12}, \hat{c}_{44}$	Independent elastic constants of $\mathbb{C}$ in the lattice frame
$\dot{\gamma}^{(\alpha)}$	Plastic slip rate on slip system α
$\dot{\gamma}_0$	Reference shearing rate
m	Instantaneous strain rate sensitivity
N	Number of slip systems
$\tau^{(\alpha)}$	Resolved shear stress on slip system α
$\dot{\tau}_c^{(\alpha)}$	Critical resolved shear stress on slip system α
τ_0	Initial critical resolved shear stress
$\mathbf{S}^{(\alpha)}$	Schmid tensor
$\theta\left(\Gamma\right)$	Work-hardening rate
$q_{\alpha\beta}$	Latent hardening matrix
θ_k	Initial hardening rate of term k
τ_k	Saturated value of hardening term k
N_τ	Number of hardening terms
ε_{eng}	Engineering strain
ε_{eq}^p	von Mises equivalent plastic strain
Γ	Accumulated plastic shear strain
$\dot{\Gamma}$	Accumulated plastic shear strain rate
t	Time
ω	Damage variable
ω_0	Initial damage
ω_c	Critical damage
q_1, q_2	Damage evolution parameters
T	Stress triaxiality ratio

Abbreviations

ED	Extrusion/reference direction
TD	Transverse direction
ND	Normal/thickness direction

the chemical composition [1, 2], heat treatment [3, 4] and mechanical processing [5, 6], one can control material properties such as the yield stress, work hardening, plastic anisotropy and ductility of an alloy [7, 8, 9]. To obtain components with the desired mechanical properties, it is crucial to understand the effects of the microstructure and the material processing on their response. One of the principal factors that affects the formability and bendability of polycrystalline metals is the crystallographic texture [10, 11, 12, 13, 14]. The crystallographic texture stems from the processing of the material, and extruded profiles and rolled

plates typically exhibit a distinct crystallographic texture. The plastic behaviour of metals and alloys is strongly influenced by the crystallographic texture, which is the primary source of plastic anisotropy [15]. The strength, work hardening, constituent particles and the grain structure can also influence the ductility and bendability of a material [16, 17].

Failure of metals during bending is usually controlled by the development of shear bands that emanate from the outer tensile surface and provide optimal paths for microcrack propagation [18, 19, 20]. The microcracks initiate in the localized zones of plastic deformation and propagate by means of conventional ductile fracture mechanisms, including nucleation, growth and coalescence of microscopic voids at constituent particles [18]. Plastic deformation leads to damage evolution as voids grow in the material due to plastic straining, and coalesce as the inter-void ligaments are subjected to plastic flow localization [21]. Damage evolution in materials can also induce strain softening and localization and thus promote ductile fracture [22]. Plastic flow and ductile fracture are coupled phenomena and the ductility of a material is strongly influenced by, e.g., its yield strength, work hardening and plastic anisotropy [23].

Since the crystal plasticity theory has an intrinsic ability to account for the crystallographic texture of materials, this theory is appropriate to use when investigating the bendability of metallic materials. Single crystal plasticity models are usually combined with different homogenization techniques to describe the behaviour of polycrystalline materials. Such homogenization techniques include: the full-constraint and relaxed-constraint Taylor models, different types of self-consistent models, and full-field micromechanical approaches [24, 25, 26, 27, 28]. In the Taylor and self-consistent homogenization models the influence of the grain structure and the inhomogeneities inside grains are not included. In contrast, the full-field methods, such as the crystal plasticity finite element method (CP-FEM), are capable of accounting for stress equilibrium and compatibility across grain boundaries, local interactions and inhomogeneities of the mechanical fields within grains, and resolving the complex grain morphology of metals and alloys [29, 30, 31, 32].

Several studies have investigated the influence of the crystallographic texture and crystal orientations on strain localization and bendability of aluminium alloys [10, 11, 12, 33]. Kuroda and Tvergaard [10] studied the effects of different texture components on shear band formation and strain localization in plane strain tension/compression and in bending using a Taylor-type crystal plasticity model. They found that the crystallographic texture of a material has a significant impact on the shear band formation in plane strain loading and bending, and that the strain at localization was drastically reduced for certain texture components compared to others. Takeda et al. [11] observed that the Taylor factor of crystals with different orientations correlated to the bendability of aluminium, and further that a low Taylor factor leads to a uniform slip deformation, while a high Taylor factor promotes shear band formation in bending. Using CP-FEM, Shi et al. [13] showed that also the texture distribution and grain size influences bendability, whereas the initial surface roughness of sheets has little effect. Westermann et al. [16] performed tensile and bending tests on three aluminium alloys with different microstructure, and found that although their tensile properties were similar, the bendability was strongly affected by the microstructure. In addition to the influence of texture, they found that the grain size and global alignment of constituent particles affected the bendability of the aluminium alloys. Saai et al. [17] used CP-FEM to explicitly model the microstructure of two aluminium alloys and found that the numerical results displayed a strong effect of the grain morphology on the bending behaviour, the surface roughness and the development of shear bands. Gorji [34] and Gorji et al. [35] performed hydraulic bulge tests and three-point bending tests and compared the results to finite element simulations, where the grain structure was modelled by distributing a varying yield stress and work-hardening behaviour. Gorji et al. [36] investigated the role of the intrinsic inhomogeneities on the post-necking deformation behaviour of an AA6016 aluminium alloy. They performed finite element simulations of tensile tests with a randomized thickness and yield stress distribution in the specimen and showed that the presence of inhomogeneities allow for a more realistic description of the localized plastic deformation including the development of shear bands. Muhammad et al. [20] modelled the formation of shear bands and fracture in bending with CP-FEM, where fracture was modelled by a critical strain criterion and element erosion. Their analyses agreed with experimental observations indicating that failure in bending is controlled by the development of shear bands and provide a minimum-energy path for microcracks to propagate. Recently, Lezaack et al. [6] used friction stir processing on an AA7475 aluminium

alloy in order to generate a fine-grained microstructure. This fine-grained microstructure showed a significant improvement in ductility under uniaxial tension loading compared to the microstructure before processing. In contrast, the crack propagation resistance in compact tension and in bending was not improved and the differences observed between the microstructures were attributed to the competition between transgranular and intergranular failure.

The aim of the present paper is to study the bendability of an aluminium alloy extruded in two different profile geometries. Suitable locations for studying the microstructure and mechanical properties are selected on exterior walls of the two profiles. Microstructural investigations reveal that the two profile materials have different grain structure but similar macroscopic crystallographic texture and constituent particle structure. Experimental tests on flat tensile specimens and bending specimens are performed, where it is found that the bendability of the two profiles is significantly different and affected by the microstructure. Crystal plasticity finite element analyses of the mechanical tests are performed to further investigate the ductile fracture process. In the simulations, each grain is explicitly modelled and the coupled damage and single crystal plasticity model of Frodal et al. [37] is used to describe damage evolution and ductile fracture. These analyses show that formation of shear bands, and thus crack initiation and propagation within these bands, depend on the grain structure, i.e., the size of the grains and the local crystallographic texture. Further, the crystal plasticity finite element simulations are able to describe the large difference in the bendability of the two profiles observed experimentally.

2. Material

The aluminium alloy 6005A is studied in this paper. The chemical composition of the alloy in weight percent is given in Table 1. This alloy has been extruded in an industrial extrusion press into two different profile geometries, presented in Figure 1. The two profiles will be denoted profile A and profile B in the following. After DC-casting, the alloy was homogenized and extruded using industrial practice. The extrusion and heat-treatment of the profiles were performed by Benteler Aluminium Raufoss AS. During the extrusion process, the profiles were cooled with maximum spray cooling, followed by forced air cooling, and stored for several days in room temperature. The profiles were then artificially aged to peak strength (temper T6), i.e., heated at 185 °C for 7 hours with a heat-up time of 2 hours to the desired temperature. After the artificial ageing, the profiles were air cooled to room temperature.

Table 1: Chemical composition of the aluminium alloy in wt% [38].

Alloy	Fe	Si	Mg	Mn	Cr	Cu	Zn	Al
6005A	0.2	0.71	0.52	0.15	< 0.05	< 0.03	< 0.2	Bal.

From the extruded profiles, two types of specimens were machined for mechanical testing, see Section 3. The locations of specimen extraction are depicted with red squares in Figure 1. The thickness of the profile walls at these locations are equal and as both locations are on an exterior wall, they are suitable for studying the differences in microstructure and mechanical properties between the two extruded profiles.

To investigate the microstructure of the materials, samples from the two profiles were mechanically ground and polished. Here we define ED to be along the extrusion direction, TD along the transverse direction and ND along the normal/thickness direction of the extruded profile. Back scattered electron (BSE) micrographs of the samples, showing the constituent particles, were taken in a Hitachi SU-6600 FESEM operated at 5.0 kV. An area of 1.12 mm^2 was investigated for each profile in the ED-ND plane, measuring a total of 9230 and 9279 constituent particles for profile A and profile B, respectively. To reveal the grain structure under polarised light in the optical microscope, polished samples were anodised at room temperature for two minutes using HBF$_4$ (fluoroboric acid). The electron back-scatter diffraction (EBSD) technique was used to obtain the grain structure and crystallographic texture, operating the Hitachi SU-6600 FESEM at 20 kV. EBSD measurements were carried out in the ED-ND and TD-ND planes of the two profiles, investigating a region of 1.2 × 4.0 mm^2 for each profile and plane, using a step size of 2 μm. This
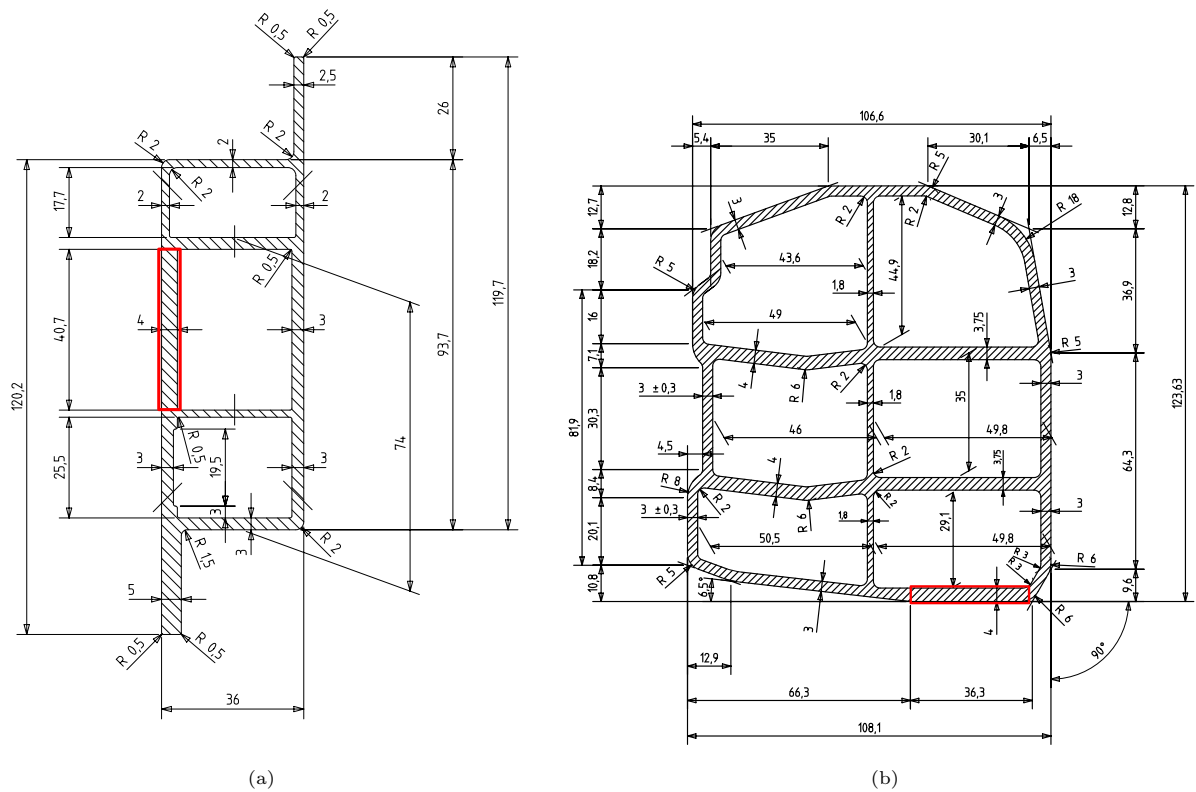
Figure 1: Geometry of the extruded profiles investigated: (a) profile A, and (b) profile B. The red squares indicate the locations of specimen extraction from the profiles. Dimensions are in mm.

region allowed for studying the entire 4 mm thickness of the profile wall. A total of 1531 and 3153 grains were measured for profile A and profile B, respectively, using a grain misorientation threshold of 5°. The EBSD data, orientation distribution function (ODF) and pole figures were calculated and plotted using the open source Matlab Toolbox MTEX [39].
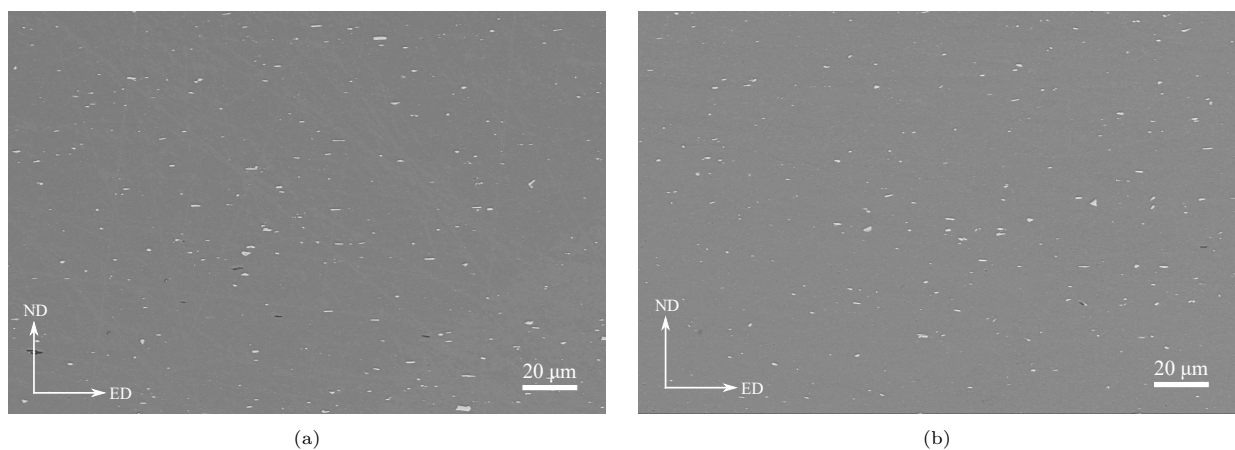
Figure 2: Distribution of constituent particles in the two profiles: (a) profile A, and (b) profile B.

Figure 2 displays BSE micrographs of the constituent particle distribution for the two profiles in the ED-

5

ND plane. The micrographs indicate that the particles are randomly distributed in the profiles with some particle clustering along ED in the form of stringers. Due to the extrusion process, the elongated particles are typically oriented with their long axis along ED. The particle distributions in the two profiles are observed to be qualitatively similar, and the measured area fraction of constituent particles is approximately $f_p \approx 0.0065$ in both profiles. The constituent particles are void nucleating particles, and play an important role in the ductile fracture process. Figure 3 presents the particle size distribution in terms of the area fraction of constituent particles versus equivalent diameter. The equivalent particle diameter is defined as $D_p = \sqrt{4A_p/\pi}$ where A_p is the measured area of the particle in the image plane. The particle size distribution has a peak for particles with equivalent diameter of approximately 1.5 µm in both profiles, and a slight variation in the particle size distributions is observed between the two profiles.
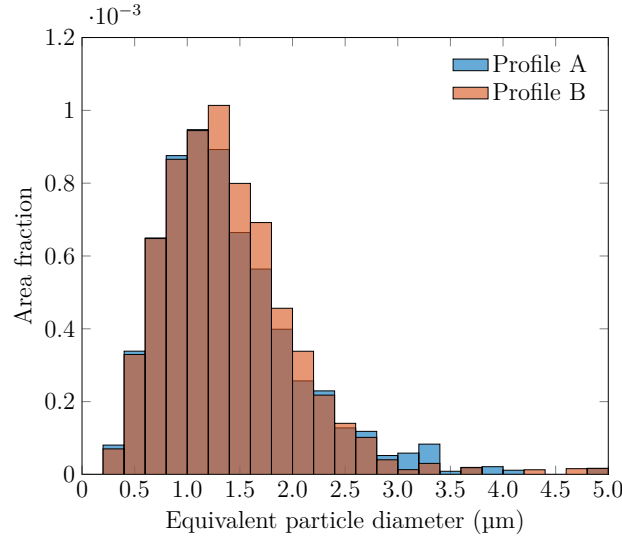

Figure 3: Particle size distribution for the two profiles in terms of area fraction of constituent particles versus equivalent diameter.

Results from the EBSD measurements in the ED-ND and TD-ND planes are depicted in Figure 4. The entire 4 mm wall thickness of the profile is scanned and presented in the figure, where the thickness of the wall is along ND. A recrystallized grain structure is found for both profiles, with a surface layer consisting of relatively small grains. A little further towards the centre of the specimen, the grains are relatively large, with larger grains observed in profile B than in profile A. In the centre of the specimens, profile A has smaller equi-axed grains with some elongated grains along ED. In contrast, profile B has a large number of tiny equi-axed grains concentrated in a smaller part of the centre region surrounded by large elongated grains. Note that the outside or inside of the profile wall is not known in relation to the EBSD measurements of Figure 4.

From Figure 4 it is quite apparent that the relative difference in the size of the small and large grains in the centre is larger for profile B than for profile A. Owing to the smaller size of the numerous grains in the centre of profile B, the measured number of grains is approximately two times higher for profile B than for profile A. As a result, the grain size represented by the area averaged equivalent diameter over the entire profile thickness is 89.2 µm for profile A and 61.4 µm for profile B. In contrast, investigating the 100 largest grains of each profile, the area averaged equivalent diameter is 255.3 µm for profile A and 308.2 µm for profile B. Whereas studying the 100 smallest grains of each profile, the area averaged equivalent diameter is 5.3 µm for profile A and 4.7 µm for profile B.

Owing to the extrusion process, the extruded profiles exhibit crystallographic texture. The pole figures for the two profiles are presented in Figure 5. Note that the macroscopic texture of the profiles are shown in the figure, i.e., the crystallographic texture comprising all the grains in the two EBSD scans of a profile. Both profiles have a crystallographic texture with components typical for a recrystallization texture, i.e., a strong
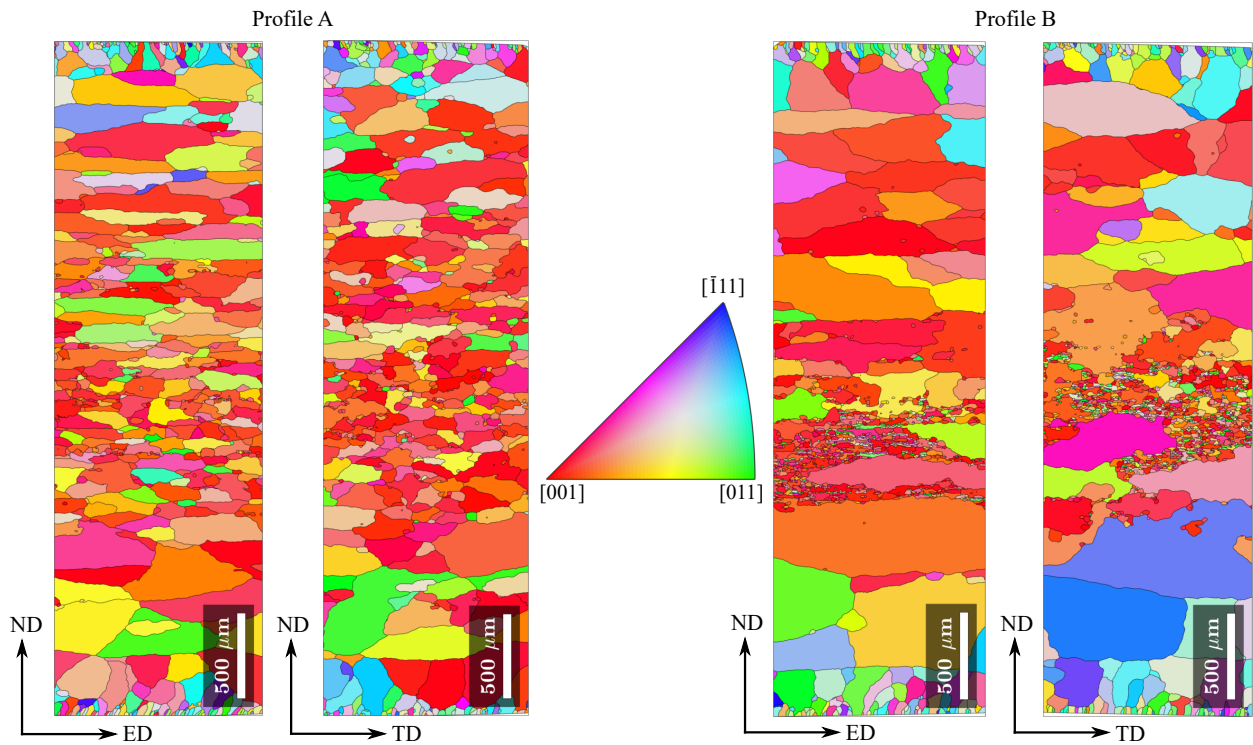
Figure 4: EBSD scans in the ED-ND and TD-ND planes of profile A (left), and profile B (right).
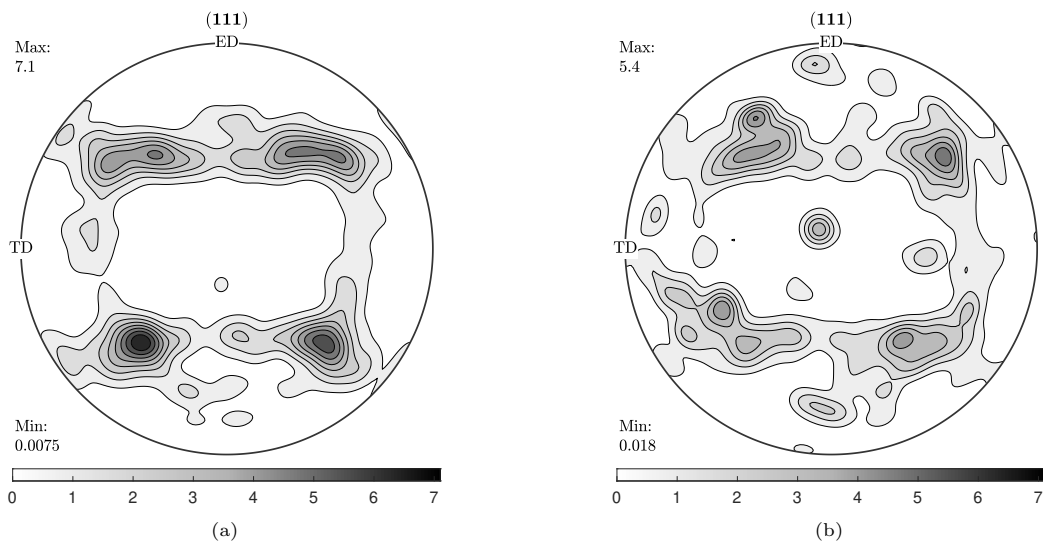

Figure 5: Pole figures (111) of the macroscopic crystallographic texture of: (a) profile A, and (b) profile B.

cube texture with a weaker Goss component. In addition, the crystallographic texture also contains a weaker rotated cube component, with an approximate 45° rotation about the ND. Albeit the crystallographic texture of the two profiles contains the same texture components, there are some differences in their intensities between the profiles, see Figure 5.

7

3. Experiments

In order to study the mechanical properties and bendability of the two profiles, mechanical tests on flat tensile specimens and bending specimens were carried out. Figure 6 shows the geometry of the two specimen types, where the width of the bending specimen was 38 mm for profile A and 32 mm for profile B. The specimens were machined from the location in the profiles indicated by the red squares in Figure 1, and the entire wall thickness was included in the samples. The tensile axis of the tensile specimens was oriented along the ED of the profiles, while the bending axis of the bending specimens coincided with the TD. Bending tests with the tension side on the exterior/outside and on the interior/inside of the profile wall were performed.
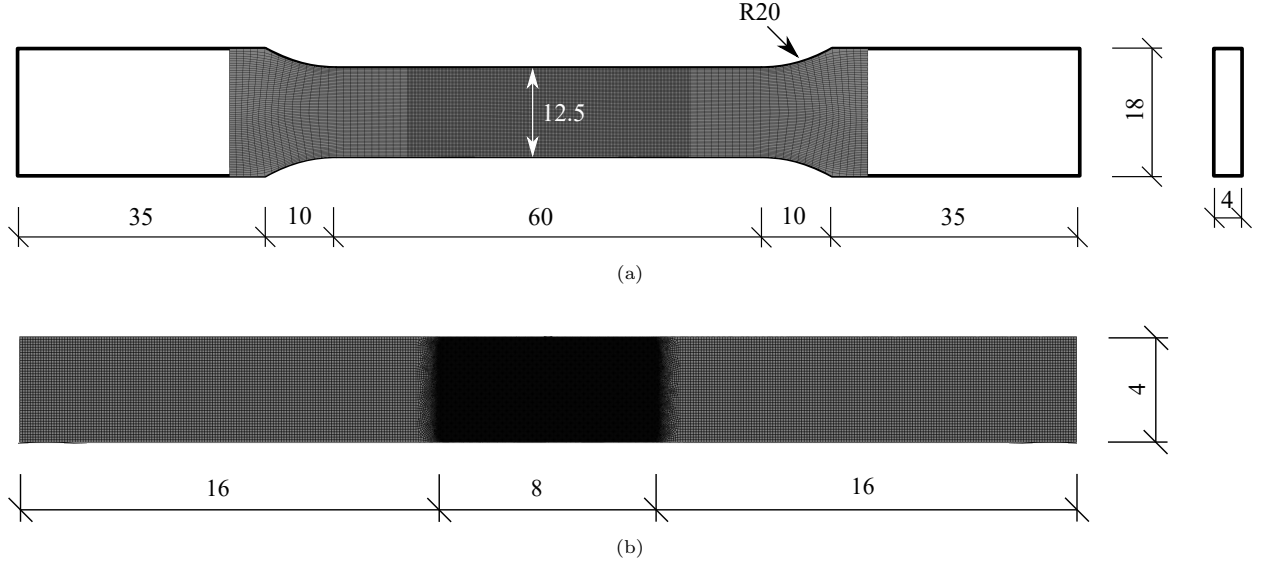

Figure 6: Specimen geometry and finite element mesh: (a) flat tensile specimen, and (b) bending specimen. The width of the bending specimen was 38 mm, and 32 mm for profile A and profile B, respectively. Dimensions are in mm.

A displacement-controlled testing machine was used to perform the experiments with a constant cross-head velocity of 0.24 mm/min in the tensile tests and 20.0 mm/min in the bending tests. Thus, the initial strain rate in the tensile tests was $0.004\ \mathrm{s}^{-1}$. The force and the displacement of the clip-on extensometer were continuously measured during the test until fracture of the tensile specimens. The clip-on extensometer was initially 40 mm long and centred on the specimen gauge section. From the measured force and extensometer displacement, the engineering stress and strain were calculated as

$$\sigma_{eng} = \frac{F}{A_0} \qquad \varepsilon_{eng} = \frac{\Delta L}{L_0} \tag{1}$$

where F is the measured force, A_0 is the initial cross-section area of the tensile specimen, ΔL is the displacement and L_0 is the initial length of the extensometer.

In the bending tests, the force F and indenter displacement u were tracked continuously during testing. A schematic representation of the bending setup is presented in Figure 7. The radius of the indenter used in these tests is 0.4 mm, and the diameter of the support rollers is $D = 30$ mm. The gap between the two rollers was two times the specimen thickness, i.e., $a = 2h = 8$ mm in accordance with the test specifications of plate bending tests for metallic materials [40]. From the measured force and dimensions of the bending specimen, the bending force per cross-section area was calculated as

$$\bar{F} = \frac{F}{wh} \tag{2}$$

where w is the width and h is the thickness of the bending specimen.
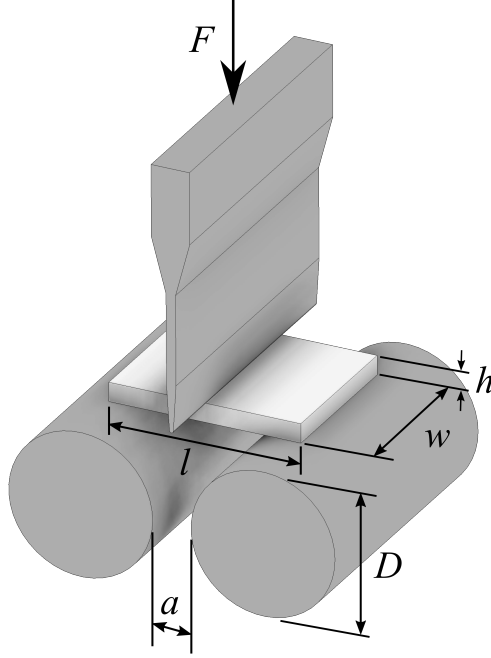
Figure 7: Bending test setup.

4. Finite element modelling

4.1. Constitutive model

Box 1: Overview of the coupled damage and single crystal plasticity model [37].

- Corotational formulation:
$$\hat{\boldsymbol{\sigma}} = \mathfrak{R}^T \cdot \boldsymbol{\sigma} \cdot \mathfrak{R} \quad \wedge \quad \hat{\mathbf{D}} = \mathfrak{R}^T \cdot \mathbf{D} \cdot \mathfrak{R} \tag{B1}$$

- Additive decomposition of the rate-of-deformation and spin tensors:
$$\mathbf{D} = \mathbf{D}^e + \mathbf{D}^p, \qquad \mathbf{W} = \mathbf{W}^e + \mathbf{W}^p \tag{B2}$$

- Evolution of the rotation tensor:
$$\dot{\mathfrak{R}} = \mathbf{W}^e \cdot \mathfrak{R} \tag{B3}$$

- Effective stress:
$$\tilde{\boldsymbol{\sigma}} = \frac{\boldsymbol{\sigma}}{1 - \omega} \tag{B4}$$

- Generalized Hooke's law on rate form:
$$\dot{\hat{\tilde{\boldsymbol{\sigma}}}} = \hat{\mathbf{C}} : \hat{\mathbf{D}}^e \tag{B5}$$

- Rate-dependent constitutive relation:
$$\dot{\gamma}^{(\alpha)} = \dot{\gamma}_0 \left| \frac{\tau^{(\alpha)}}{(1 - \omega)\,\tau_c^{(\alpha)}} \right|^{\frac{1}{m}} \mathrm{sgn}\left(\tau^{(\alpha)}\right) \tag{B6}$$

- Resolved shear stress:
$$\tau^{(\alpha)} = \boldsymbol{\sigma} : \mathbf{S}^{(\alpha)} = \hat{\boldsymbol{\sigma}} : \hat{\mathbf{S}}^{(\alpha)} \tag{B7}$$

- Critical resolved shear stress:
$$\dot{\tau}_c^{(\alpha)} = \theta\left(\Gamma\right) \sum_{\beta=1}^{N} q_{\alpha\beta} \left| \dot{\gamma}^{(\beta)} \right| \tag{B8}$$

- Work-hardening rate:
$$\theta\left(\Gamma\right) = \sum_{k=1}^{N_\tau} \theta_k \exp\left(-\frac{\theta_k}{\tau_k}\Gamma\right) \tag{B9}$$

- Accumulated plastic shear strain:
$$\Gamma = \int_0^t \sum_{\alpha=1}^{N} \left| \dot{\gamma}^{(\alpha)} \right| dt \tag{B10}$$

- Evolution of damage:
$$\dot{\omega} = \frac{3}{4} q_1 q_2 \omega \left(1 - \omega\right) \sinh\left(\frac{3}{2} q_2 T\right) \dot{\Gamma} \tag{B11}$$

An overview of the coupled damage and single crystal plasticity model [37] used in this study is presented in Box 1. The model introduces damage in the constitutive relation by an effective stress tensor, and can describe typical phenomena encountered in ductile fracture, such as damage induced strain softening, heterogeneous damage and deformation fields, strain localization and shear banding, effects of the

9

crystallographic texture and grain structure on the ductile fracture strain, crack propagation in single and polycrystalline materials and serrated fracture surfaces. The numerical implementation of the model utilizes a hypo-elastic formulation [41], where it is assumed that the elastic deformations are infinitesimal, while rotations and the plastic deformations can be finite. For a damage variable of zero, the model reduces to a regular rate-dependent single crystal plasticity model [25]. Another important class of crystal plasticity models with damage are the single crystal porous plasticity models, e.g., [42, 43, 44]. The model used in this study [37] is selected due to its numerical efficiency, making it able to be used in polycrystalline finite element simulations with a relatively large number of grains and a fine discretization of the microstructure.

4.2. Finite element models

The coupled damage and single crystal plasticity model described above is implemented into a user material subroutine (VUMAT) [41] for Abaqus/Explicit. The model will be used in finite element simulations of the tensile and bending tests of the two profiles described in Section 2. An explicit integration scheme is utilized for time integration of the rate constitutive equations of single crystal plasticity [37], along with explicit integration of the momentum equations. The user material subroutine has been made open source by the authors, see [41].

The finite element mesh of the tensile specimen is shown in Figure 6a. Linear eight-node elements with selective reduced integration (C3D8) are used, where the dimension of the centre-most elements is $200 \times 200 \times 200$ µm^3 for the tensile specimen. Extensive testing with different finite element meshes showed that the macroscopic response is largely unaffected by variations in the element size, as long as the element size is kept relatively small, i.e., in the same order of magnitude as the grain size [37]. Due to the failure mode of the flat tension test the entire specimen is modelled. Mass scaling is used to reduce the computational time, and it is ensured that the response is quasi-static, i.e., that the kinetic energy is negligible compared with the internal energy. The appropriate displacement controlled loading is applied to the end of the tensile specimen. All grains in the model, where each grain is represented by a single element, are given initial orientations to account for the crystallographic texture of the two profiles. The crystal orientations are generated using the open source Matlab toolbox MTEX [39]. For the tensile specimen, the orientation distribution function (ODF) is used to generate a set of orientations representing the texture of each profile. Thus, it is ensured that the crystallographic texture of the finite element model of the specimen is as close as possible to the texture measured with EBSD.

Figure 6b presents the finite element mesh of the bending specimen. Linear eight-node elements with selective reduced integration (C3D8) are used, where the dimension of the centre-most elements is $20 \times 20 \times 100$ µm^3 for the bending specimen. The longest element side is along the bending axis, i.e., along TD. Due to the approximate plane-strain condition during bending, only a 100 µm slice of the bending specimen is modelled to reduce the computational time, and the finite element model is constrained with plane-strain boundary conditions along TD. An analytic rigid indenter is used to apply the load onto the bending specimen, where a surface-to-surface contact formulation is used between the specimen, the rigid indenter and the rigid support rollers, see Figure 7 for a visualization of the bending test setup. A friction coefficient of 0.05 is used between the indenter and the specimen, whereas a friction-less formulation is used for contact between the rollers and the bending specimen.

For the bending specimens, the grain structure and the crystallographic orientations measured with EBSD are used to generate the microstructure of the finite element model using MTEX [39] and Texture2Abaqus [45]. The EBSD scans in Figure 4 are mirrored and repeated to cover the entire bending specimen, and each finite element is given the orientation of the grain corresponding to its location in the mirrored and repeated EBSD scan. By this approach, the microstructure of the bending specimen is representative for the microstructure found for the two profiles. Figure 8 displays the distribution of grain orientations in the finite element models of the bending specimens for the two profiles. Bending tests with the tension side on the outside wall and on the inside wall were performed, thus simulations with the microstructure turned up-side-down (rotated 180°) to Figure 8 were also carried out.

Table 2 contains the crystal plasticity parameters controlling the elastic behaviour, the rate dependence and the self- and latent hardening, which are common for a broad range of aluminium alloys found in the
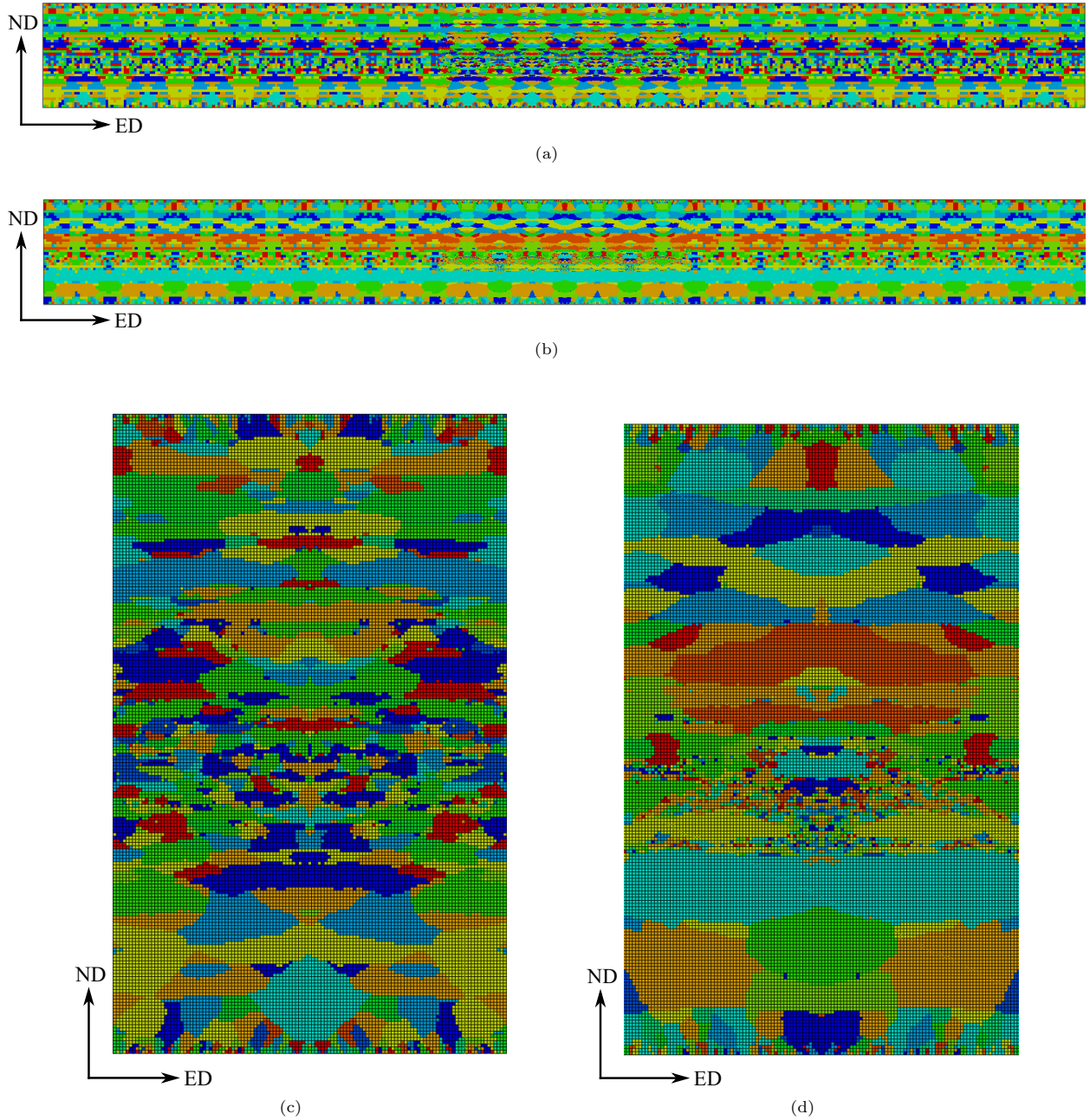
Figure 8: Distribution of grain orientation in the finite element models of the bending specimens from the two profiles: (a) entire profile A, and (b) entire profile B, (c) centre section of profile A with the finite element mesh, (d) centre section of profile B with the finite element mesh, depicted in the ED-ND plane. The Euler angle φ_1 (Bunge convention) is represented in different colours. The sets of Euler angles are extracted from the EBSD scans in Figure 4, which have been mirrored and repeated to cover the entire bending specimen. The orientations of the microstructure are the same as in the EBSD measurements of Figure 4.

literature [37]. These parameters are assumed constant in this study, while the parameters governing initial slip resistance, work hardening, damage and failure are dependent upon the material.

The initial slip resistance and work hardening parameters, given in Table 3, are calibrated to the experimental results of the tensile tests by inverse modelling. Since the distribution of constituent particles

11

Table 2: Crystal plasticity parameters governing elasticity, rate sensitivity and latent hardening for the aluminium alloy [37].

$\hat{c}_{11}$ (MPa)	$\hat{c}_{12}$ (MPa)	$\hat{c}_{44}$ (MPa)	$\dot{\gamma}_0$ (s^{-1})	m	$q_{\alpha\beta}$
106 430	60 350	28 210	0.010	0.005	1.0 if $\alpha = \beta$ 1.4 if $\alpha \neq \beta$

Table 3: Crystal plasticity parameters governing initial slip resistance, work hardening, damage evolution and failure for the two profiles.

Profile	τ_0 (MPa)	θ_1 (MPa)	τ_1 (MPa)	θ_2 (MPa)	τ_2 (MPa)	ω_0	ω_c	q_1	q_2
Profile A	118.7	−404.0	−6.3	131.0	10.0	0.0065	0.40	1.5	1.0
Profile B	118.7	−500.8	−7.0	80.0	7.0	0.0065	0.40	1.5	1.0

is similar in the two profiles consisting of the same aluminium alloy, it is a reasonable conjecture that the damage parameters of the two profiles will be similar. Thus, the damage and failure parameters of the two profiles are set to be equal. The initial damage ω_0 of the profiles is taken equal to the area fraction of constituent particles so that $\omega_0 = f_p \approx 0.0065$, see Section 2. The parameters q_1 and q_2 are set to their default value of 1.5 and 1.0, respectively. These values are similar to the values proposed by Tvergaard [46] for the Gurson [47] model. The last damage parameter ω_c is set to a reasonable value so that fracture in the experiments and finite element analyses of the tensile tests occurs at approximately the same time. Fracture is modelled by element erosion and an element is deleted when $\omega = \omega_c$ in one of the element's integration points.

5. Results

The engineering stress-strain curves from the experimental tests and the crystal plasticity finite element analyses of the flat tensile specimen are shown in Figure 9. Comparing the initial yield strength of the two profiles, it is found that profile A has a slightly lower initial strength than profile B. This is despite the fact that they have the same initial critical resolved shear stress τ_0, see Table 3; thus indicating a slight variation of the Taylor factor due to minor texture differences in the two profiles. Further, the work-hardening behaviour appears to be similar, with the point of necking occurring a little earlier for profile B than for profile A. The reduction in the stress level after necking and prior to fracture is also similar in the two profiles. Figure 9 further shows that the response of the finite element analyses gives similar trends as observed experimentally.

Figure 10 displays the force-displacement curves from the bending tests. The initial force levels of the two profiles are similar, with the force being a little lower for profile B than for profile A. This is in contrast to the tensile tests where the initial yield strength was slightly lower for profile A than for profile B. The cause of this difference is the difference in the crystallographic texture of the two profiles, see Figure 5, and a difference in the Taylor factor for the two deformation modes. Further, it is seen that the bendability of the two profiles is significantly different, i.e., the displacement at failure for profile B is only half the displacement of profile A at failure. The crystal plasticity finite element simulations capture this difference in the bendability of the two profiles, and the simulations are in good agreement with the experiments when predicting a much higher bendability of profile A than of profile B. Considering the difference in bendability between the "outside" and "inside" bending tests, i.e., the bending tests with the tension side on the outside wall or on the inside wall, we find that the inside bending tests typically have a higher bendability than the outside bending tests for profile A, whereas for profile B the trend is opposite. The difference in the displacement at failure is larger for profile A than for profile B, which is captured by the finite element simulations by rotating the grain structure 180°. The orientation of the grain structure shown in Figure 8, gives the highest bendability of profile A and the lowest of profile B in the finite element simulations.
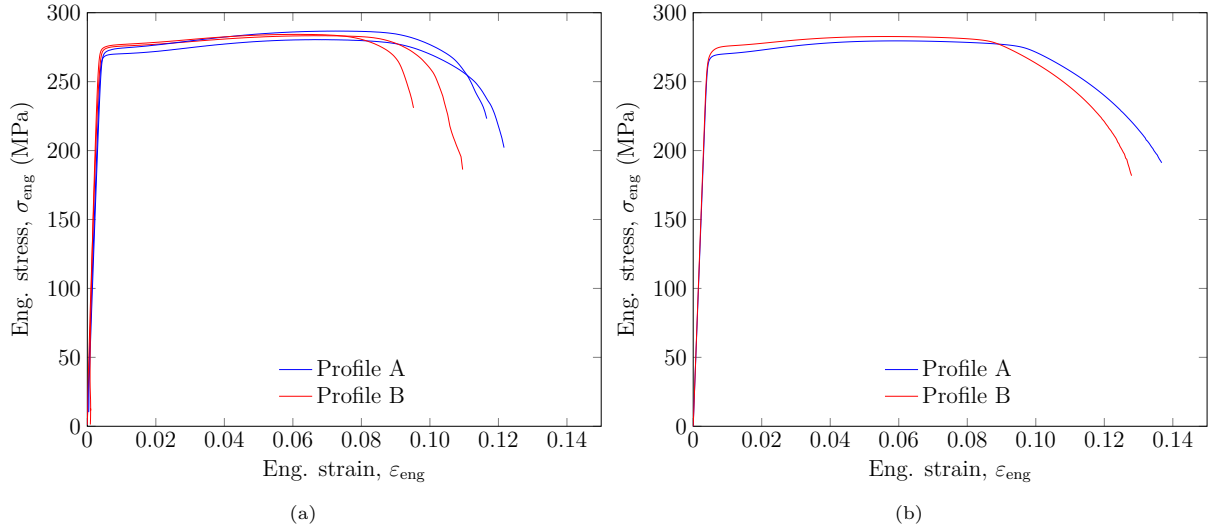
12

Figure 9: Engineering stress-strain curves from tensile tests of the two profiles: (a) experiments, and (b) finite element analyses.
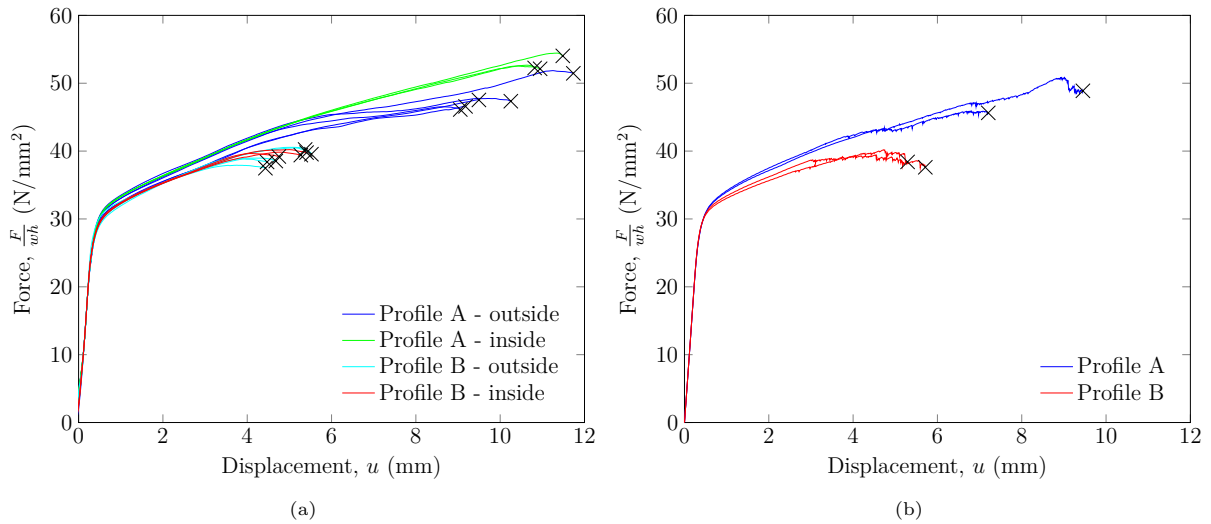

Figure 10: Force-displacement curves from bending tests of the two profiles: (a) experiments, and (b) finite element analyses. Bending tests with the tension side on the outside wall and on the inside wall were performed. The orientation of the grain structure shown in Figure 8 gives the highest bendability of profile A and the lowest of profile B in the finite element simulations.

Figure 11 presents the centre of the gauge section of the tensile specimen at different stages during the deformation process from the crystal plasticity finite element analyses. Contours of the von Mises equivalent plastic strain are depicted on the surface of the simulated specimen. The von Mises equivalent plastic strain is defined as

$$\varepsilon_{eq}^p = \int_0^t \sqrt{\frac{2}{3}\mathbf{D}^p : \mathbf{D}^p} dt \tag{3}$$

Due to differences in the crystallographic orientation between grains, the local deformation is heterogeneous, creating shear bands which can be observed as contours on the exterior of the specimen. These shear bands form early in the deformation process and persist until fracture. This is consistent with experimental evidence found using in situ synchrotron laminography imaging of notched flat samples [48]. As individual grains with distinct orientations will rotate and deform differently, a roughness – or orange peel – develops

13

on the surface of the specimen. With straining, the deformation is observed to localize in a slant plastic strain band for both profiles. After failure, elements start to erode from the centre of the specimen where the stress triaxiality and the damage variable are at their maximum. The crack formed by element erosion then propagates towards the edge of the specimen and the stress level drops rapidly. Finally, the specimen is separated into two halves with a slanted fracture surface observed for both profiles.
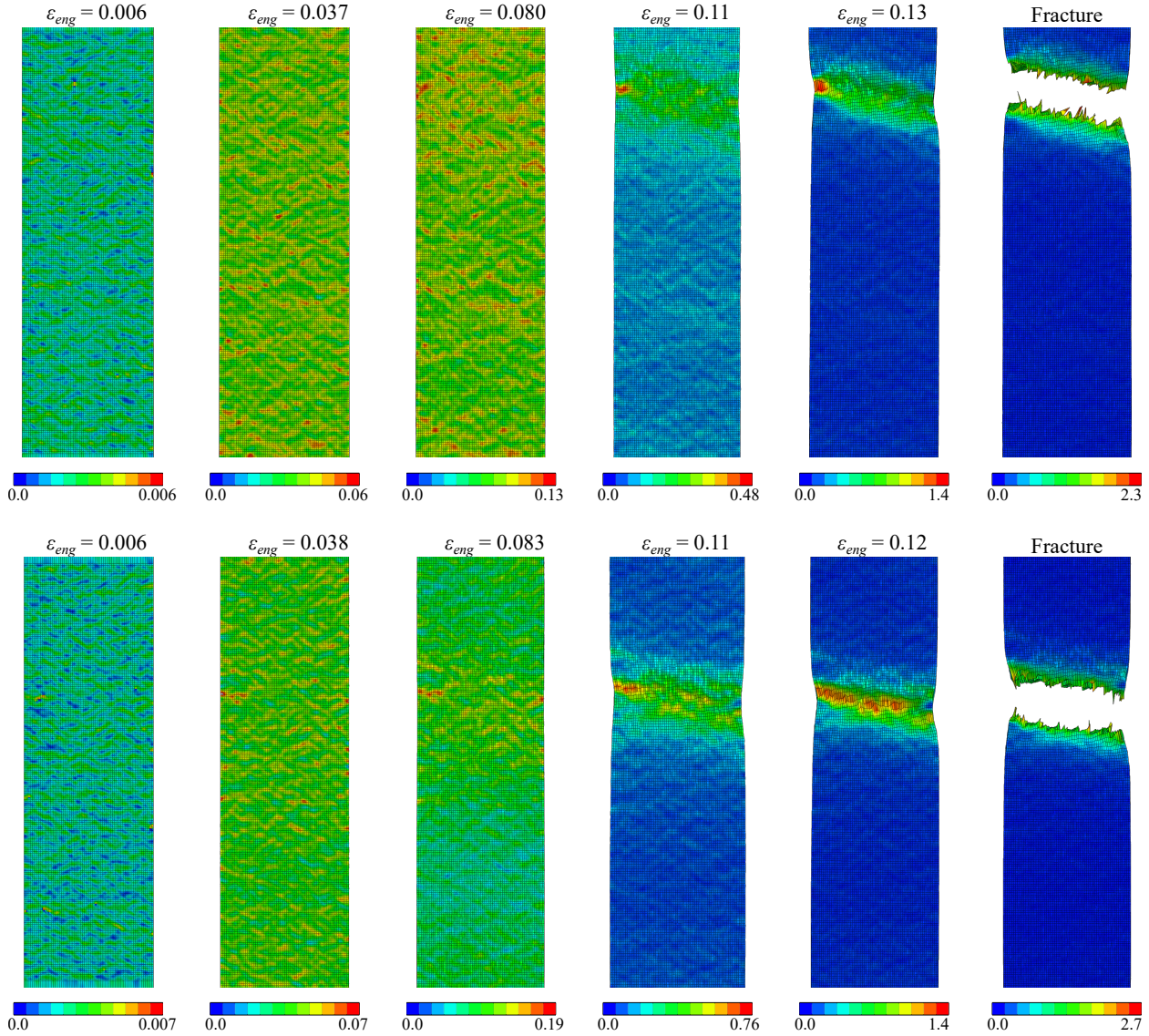

Figure 11: Deformed configuration plots from the centre of the gauge section of the tensile specimen at different stages during the deformation process from the finite element analyses depicted in the ED-TD plane for: profile A (top), and profile B (bottom). Contours of the von Mises equivalent plastic strain are shown on the deformed meshes and the corresponding engineering strain is depicted above each mesh.

The fracture surfaces of the tensile tests predicted by the crystal plasticity finite element analyses for the two profiles are shown in Figure 12. Due to the heterogeneous deformation field caused by discrete grains with different orientations, the edges of the specimen surface have a clear surface roughness. A non-symmetric fracture surface is also observed for both profiles, as the local texture will be slightly different at unique locations in the specimen. A typical fracture surface shape for flat tensile specimens is observed, where the contraction of the specimen is larger in the middle of the specimen than towards the edges and

14

corners of the cross-sectional area. The ductility of the two profiles are comparable as the area of the fracture surface is similar. Thus, when the grain structure and damage variables of the two profiles are equal, the tensile ductility predicted by the finite element simulations is similar in the two cases.
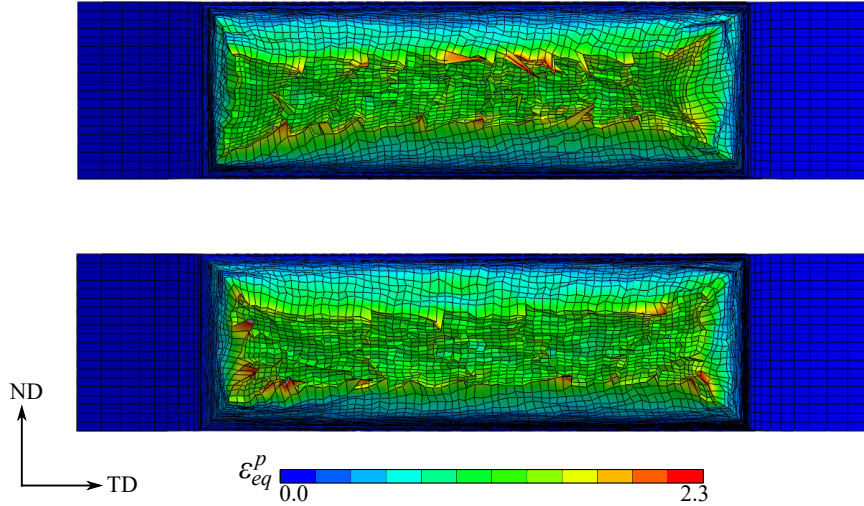

Figure 12: Fracture surfaces of the tensile specimen predicted by the crystal plasticity finite element analyses with contours of the von Mises equivalent plastic strain for: profile A (top), and profile B (bottom).

In Figure 13 and Figure 14, the deformation process from the finite element simulations of the bending specimen for the two profiles is presented. We find that shear bands form early during the deformation process for both profiles, with the highest values of the von Mises equivalent plastic strain on the top and bottom of the bending specimen. Initially, the deformation field and shear bands are quite dispersed and numerous. As the deformation continues, the deformation appears to localize in fewer deformation bands. Fracture is first observed in one of these deformation bands on the bottom of the bending specimen for both profiles.

Comparing the deformation fields of the two profiles it is apparent that the distribution of plastic deformation and strain localization are different in the two. Profile A appears to distribute the plastic deformation over a larger area and more evenly than profile B. These differences are caused by the differences in the grain structure and the local grain orientations in the finite element models that come from the EBSD measurements. The first sign of fracturing is observed after a 5 to 6 mm displacement of profile A, whereas a small crack is observed in profile B after only 4 mm displacement. With further deformation, profile A appears to be more resistant to crack initiation and propagation than profile B. For profile A, only a small crack develops in the surface layer of the bending specimen that is arrested before it starts to grow again at a displacement of approximately 8 to 9 mm. In contrast, the crack formed quite early in the surface layer of profile B continues to grow with further deformation and a large crack, through more than half of the bending specimen, is observed after only 6 mm displacement. Considering the crack pattern developed in the two profiles, we find that a saw-blade pattern develops which is typically observed in experimental tests.

The deformed grain structure from the centre of the bending specimen after testing from the experiments and finite element simulations is presented in Figure 15. Cracks running through the centre of the specimens are observed both in the experiments and numerical analyses, and are best visible for profile A in the experimental test specimens. Inspecting the crack paths in the different specimens, the crack follows both grain boundaries and runs across the interior of grains. It appears that the crack initiates at the specimen surface and propagates along or in the neighbourhood of a grain boundary. Then, as the crack has propagated through the surface layer of the bending specimen, the crack seems to be more likely to go through the grain interior. The location of crack initiation and the crack path chosen for the different profiles and specimens appear to be dependent of the grain structure, and different crack paths are seen in all of the specimens for
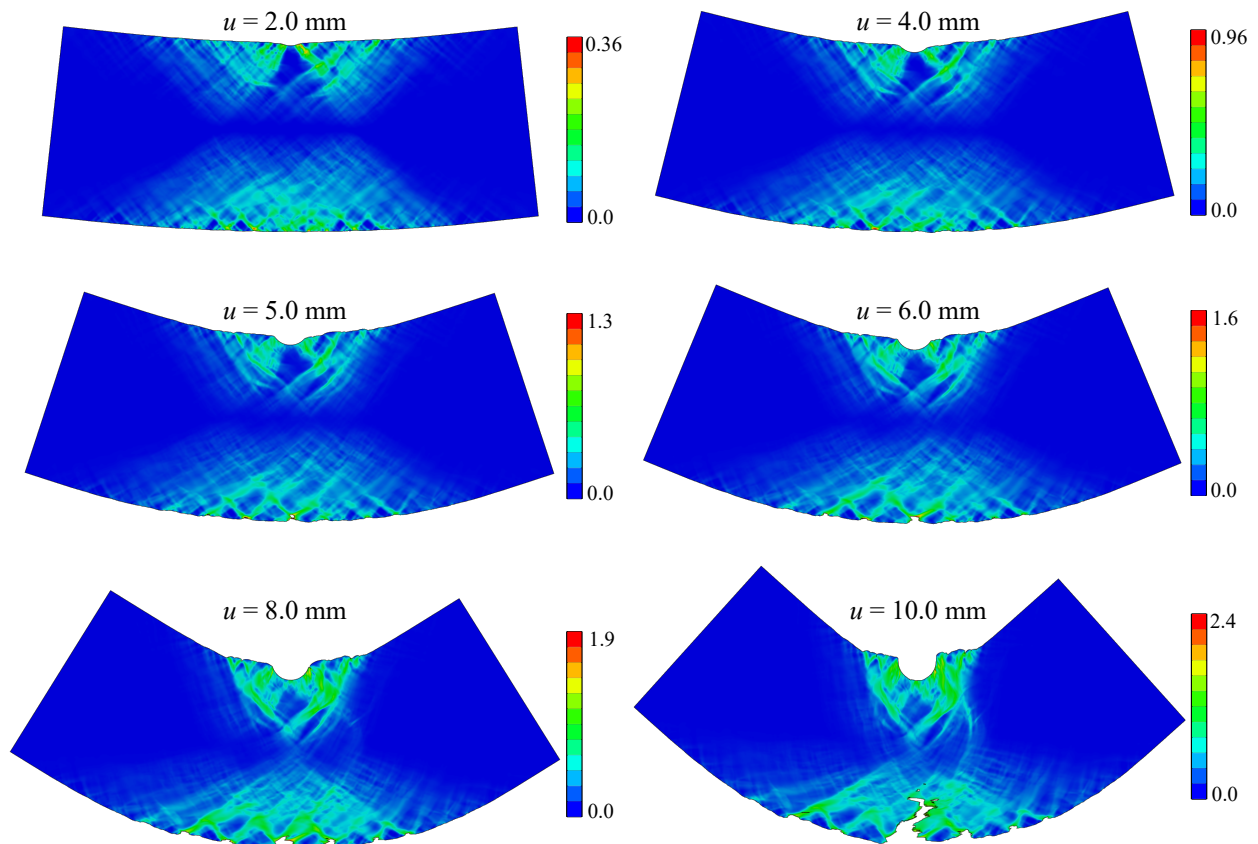
15

Figure 13: Deformed configuration plots of the centre of the bending specimen at different stages during the deformation process from the finite element analyses depicted in the ED-ND plane for profile A. Contours of the von Mises equivalent plastic strain are shown on the deformed meshes and the corresponding displacement is depicted above each mesh. The grain structure is oriented as shown in Figure 8a.

both the experiments and numerical analyses. Further, the difference in bendability between profile A and profile B observed in Figure 10 is also seen here, as the bending angle of the tested specimens is different for the two profiles after testing.

6. Discussion

In the tension tests, a similar tensile ductility is found for the two profiles, see Figure 9. A small difference in the work-hardening behaviour of the two profiles affects the point of necking which appears a little earlier for profile B than for profile A. Albeit the tensile ductility of the two profiles is similar, their bendability is significantly different and affected by the microstructure. This is in agreement with the results of Westermann et al. [16] who found differences in the bendability of 7000-series aluminium alloys with similar tensile properties. They found that the bendability was strongly dependent on the microstructure and the global alignment of constituent particles. In the present investigation, the arrangement of constituent particles and their size distribution are similar for the two profiles, with the major difference between the two profiles being their grain structure.

The displacement at failure in the bending tests of profile A is approximately two times as large as for profile B, see Figure 10. This difference is attributed to the markedly different grain structure observed for the two profiles, see Figure 4, as their other material properties are rather similar. Profile B has a larger variation in the grain size across the thickness than profile A. The large grains in profile B are larger than
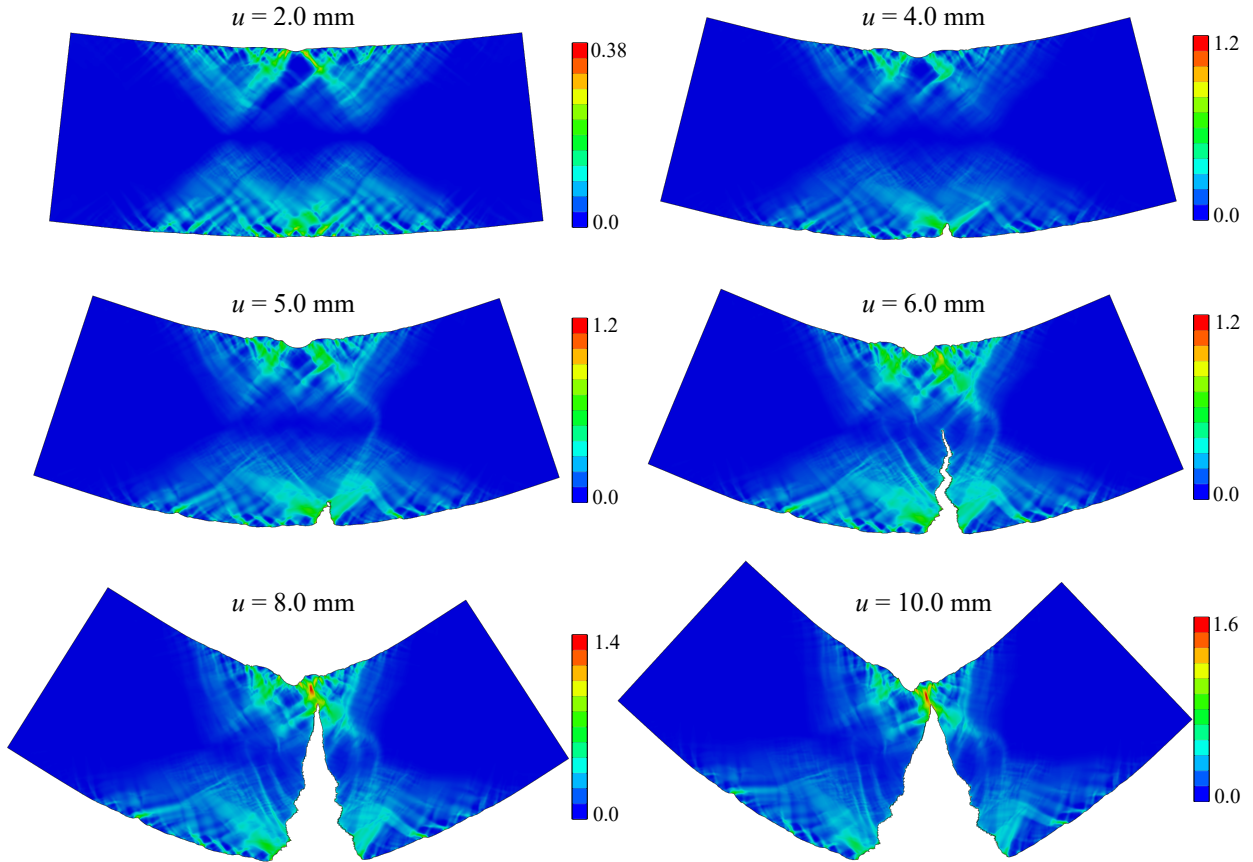
16

Figure 14: Deformed configuration plots of the centre of the bending specimen at different stages during the deformation process from the finite element analyses depicted in the ED-ND plane for profile B. Contours of the von Mises equivalent plastic strain are shown on the deformed meshes and the corresponding displacement is depicted above each mesh. The grain structure is oriented as shown in Figure 8b.

the large grains in profile A and the small grains are smaller. During bending, these differences in the grain structure will affect the shear band formation as observed in Figure 13 and Figure 14. The bimodal grain structure of profile B with large grains next to the surface layers and small grains in the centre is detrimental to the bendability as the plastic flow localizes in fewer shear bands, thus resulting in higher strain levels in these bands. This accelerates the ductile damage process inside of these localization bands and promotes ductile fracture.

As the strain localizes in plastic shear bands emanating from the surface to the centre of the specimen, these bands traverse numerous grains in the bending specimen. These grains have different crystallographic orientations that affect the stress state inside of the band, thus the damage process is influenced by the orientation of the grains inside of the localization band. This can result in a heterogeneous damage process that develops faster in certain favourable grains as the void-induced damage grows due to plastic straining. Thus, when a crack is formed on the surface of the specimen it might arrest as the resistance for damage growth and crack propagation is higher in the neighbouring grains, as observed for profile A in Figure 13. The higher resistance to crack formation and propagation in certain grains, depending on their crystallographic orientations, affects also the strain to fracture in these grains. It is therefore important to include an accurate ductile damage model in these types of crystal plasticity simulations for a precise description of ductile fracture and crack propagation in bending.

The microstructure used in the crystal plasticity finite element analyses of the bending specimen has
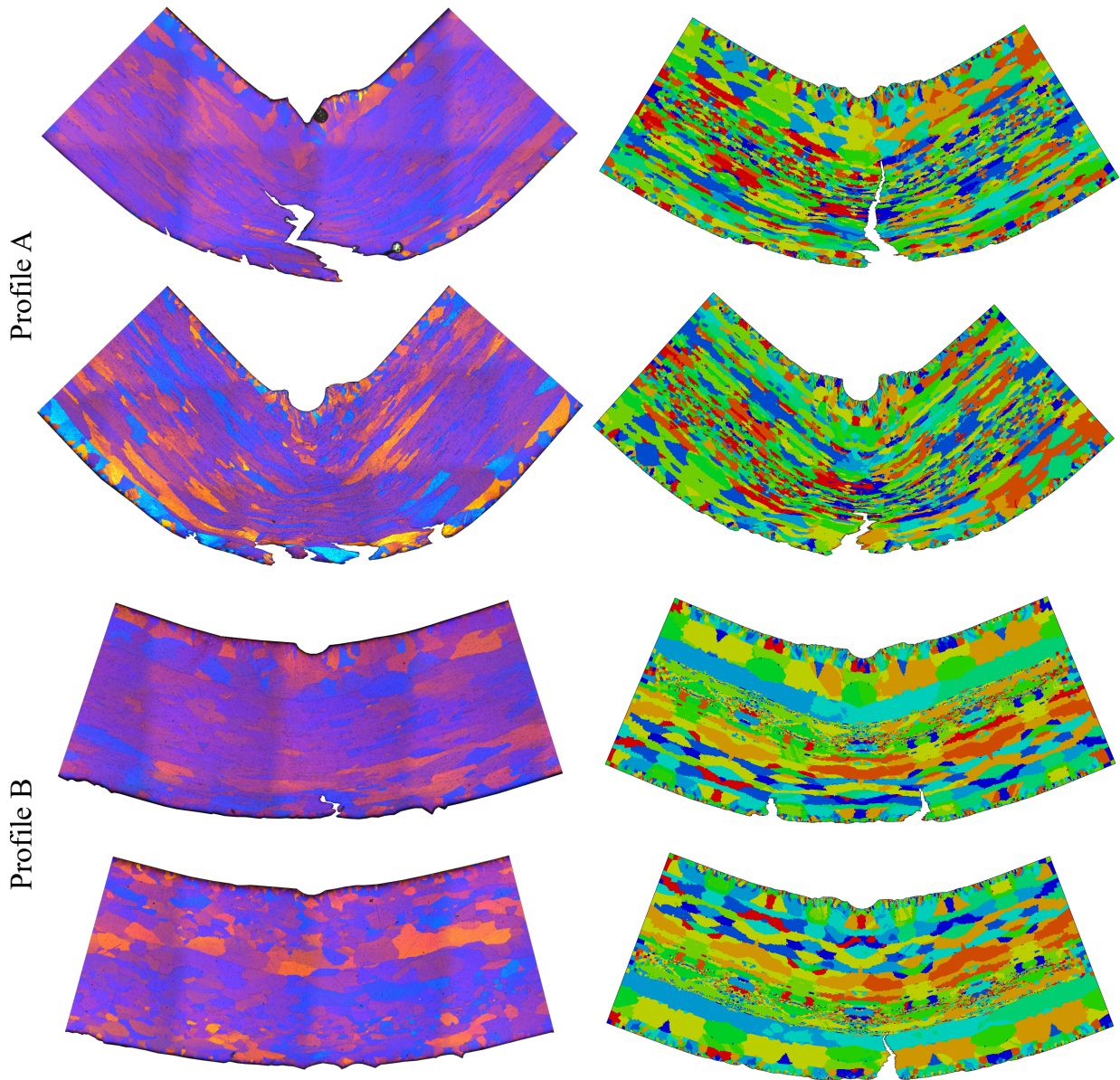
Figure 15: Deformed grain structure of the centre of the bending specimen after testing depicted in the ED-ND plane for profile A (top), and profile B (bottom), experiments (left) and the crystal plasticity finite element analyses (right) with the Euler angle φ_1 represented in different colours. The experimental bending test with the tension side on the inside wall for a profile is displayed above the test with the tension side on the outside wall. For the finite element analyses the same microstructure is used for the two tests of a profile, but the grain structure is rotated 180° in one of the cases.

been generated using the EBSD measurements performed on a 1.2×4.0 mm^2 area over the entire thickness of the specimen. Due to the large grains of profile B, a small number of grains are represented along the shortest measurement axis, i.e., along ED, and in Figure 4, the ED-ND scan of profile B displays one grain being larger than 1.2 mm along ED. Thus, when generating the microstructure of the bending specimen by use of mirroring and repeating the EBSD measurement, this grain will be abnormally large along ED, see Figure 8. In contrast, a large number of grains are represented along ED for profile A. The influence of this method in generating the microstructure on the response of the bending tests is dependent on the

18

EBSD measurement area, the grain size and the distribution of deformation during bending. Based on the distribution of the plastic shear bands depicted in Figure 13 and Figure 14, the region subjected to severe plastic deformations is found to be limited. Thus, it is a reasonable conjecture that there is only a minor influence of this microstructure generation method on the response of the bending tests with the crystal plasticity finite element method in this study.

A plane strain boundary condition is assumed in this study and the grain structure of the bending specimen is represented by a plane strain slice of the microstructure. In the real profile materials, the microstructure will be three-dimensional with the grain boundary normals not always lying in the ED-ND plane. Thus, neighbouring grains along TD can also influence the formation of shear bands and plastic deformation as these grains can promote or restrict plastic localization and damage growth due to their different crystallographic orientation relative to their neighbours. Albeit, not accounting for this three-dimensional microstructure, the crystal plasticity analyses performed herein are capable of predicting the relatively large difference in the bendability of the two profiles observed experimentally.

The precipitation free zones (PFZs) located adjacent to the grain boundaries in age hardenable aluminium alloys are thought to be important for strain localization and ductile fracture. In these zones, the plastic deformation can localize, and crack initiation and growth may occur more easily [49, 50]. The PFZs may also develop significant misorientations relative to their parent grains as the deformation localizes in these zones, which in turn could contribute to the strengthening of the PFZs [51] and thus also delay fracture initiation. The width of the PFZs is typically from a few tens to some hundreds of nanometre and depends markedly on the cooling rate after the solution heat-treatment [9]. Owing to their tiny scale, they are impossible to explicitly include in modelling of engineering specimens with the computational resources available today. Because of their influence on ductile fracture, the PFZs may also affect the bendability of age hardenable aluminium alloys. The role of the PFZs in the ductile fracture process is still an open question and further research on this topic is needed.

7. Concluding remarks

A 6005A aluminium alloy extruded in two profile geometries was studied by conducting experimental tests on flat tensile specimens and bending specimens. The materials in the two profiles had different grain structure, but similar macroscopic crystallographic texture and constituent particle structure. From the tensile tests, the work-hardening behaviour of the two profiles was similar, but the point of necking was observed to occur a little earlier for profile B than for profile A. The tensile ductility of the two profiles was also comparable as the reduction of the nominal stress level after necking was similar. Albeit small variations were observed in the tensile properties of the two profiles, their bendability was markedly different, i.e., the displacement at failure for profile A was two times higher than the displacement of profile B at failure.

Crystal plasticity finite element simulations of the mechanical tests were conducted where each grain was explicitly included in the models of the tensile and bending specimens. From the analyses of the tensile tests, a heterogeneous plastic strain field with shear bands was observed, and after diffuse necking a slanted localization band occurred, creating a slanted fracture surface for both profiles. The crystal plasticity analyses of the bending specimen captured the difference in the bendability of the two profiles, and the finite element simulations were in good agreement with the experiments in predicting a considerably higher bendability of profile A.

The large difference in the bendability of the two profiles is largely attributed to the shear band formation in the profiles, which is determined by the grain structure and the crystallographic orientation of grains in the area subjected to bending. In these bands of localized plastic deformation, the conditions are optimal for damage evolution and they serve as prime locations for crack initiation and propagation. Certain grains located in these shear bands may also have a higher resistance to damage evolution due to their crystallographic orientation and a propagating crack may be arrested before it starts to propagate again with further straining or it may change direction as it finds a more favourable path for propagation. Thus, for an accurate description of crack initiation and propagation in bending tests of metals and alloys, a simulation model able to account for the complex interactions of the grain structure, crystallographic texture, stress state and plastic deformation on the damage process is required.

19

Acknowledgements

References

[1] C. D. Marioara, S. J. Andersen, H. W. Zandbergen, R. Holmestad, The influence of alloy composition on precipitates of the Al-Mg-Si system, Metallurgical and Materials Transactions A 36 (2005) 691–702.

[2] M. S. Remøe, K. Marthinsen, I. Westermann, K. Pedersen, J. Røyset, C. Marioara, The effect of alloying elements on the ductility of Al-Mg-Si alloys, Materials Science and Engineering: A 693 (2017) 60–72.

[3] A. Deschamps, G. Texier, S. Ringeval, L. Delfaut-Durut, Influence of cooling rate on the precipitation microstructure in a medium strength Al–Zn–Mg alloy, Materials Science and Engineering: A 501 (2009) 133–139.

[4] K. Strobel, M. D. H. Lay, M. A. Easton, L. Sweet, S. Zhu, N. C. Parson, A. J. Hill, Effects of quench rate and natural ageing on the age hardening behaviour of aluminium alloy AA6060, Materials Characterization 111 (2016) 43–52.

[5] M. B. Lezaack, F. Hannard, L. Zhao, A. Orekhov, J. Adrien, A. Miettinen, H. Idrissi, A. Simar, Towards ductilization of high strength 7XXX aluminium alloys via microstructural modifications obtained by friction stir processing and heat treatments, Materialia 20 (2021) 101248.

[6] M. B. Lezaack, F. Hannard, A. Simar, Understanding the ductility versus toughness and bendability decoupling of large elongated and fine grained Al 7475 - T6 alloy, Materials Science and Engineering: A 839 (2022) 142816.

[7] K. V. Yang, P. Rometsch, C. H. J. Davies, A. Huang, X. Wu, Effect of heat treatment on the microstructure and anisotropy in mechanical properties of A357 alloy produced by selective laser melting, Materials & Design 154 (2018) 275–290.

[8] T. Nakata, C. Xu, R. Ajima, Y. Matsumoto, K. Shimizu, T. T. Sasaki, K. Hono, S. Kamado, Improving mechanical properties and yield asymmetry in high-speed extrudable Mg-1.1Al-0.24Ca (wt%) alloy by high Mn addition, Materials Science and Engineering: A 712 (2018) 12–19.

[9] B. H. Frodal, E. Christiansen, O. R. Myhr, O. S. Hopperstad, The role of quench rate on the plastic flow and fracture of three aluminium alloys with different grain structure and texture, International Journal of Engineering Science 150 (2020) 103257.

[10] M. Kuroda, V. Tvergaard, Effects of texture on shear band formation in plane strain tension/compression and bending, International Journal of Plasticity 23 (2007) 244–272.

[11] H. Takeda, A. Hibino, K. Takata, Influence of Crystal Orientations on the Bendability of an Al-Mg-Si Alloy, Materials Transactions 51 (2010) 614–619.

[12] S. Ikawa, M. Asano, M. Kuroda, K. Yoshida, Effects of crystal orientation on bendability of aluminum alloy sheet, Materials Science and Engineering: A 528 (2011) 4050–4054.

[13] Y. Shi, H. Jin, P. D. Wu, D. J. Lloyd, On the study of the sheet bendability in AA5754-O temper alloy, Metallurgical and Materials Transactions A 47 (2016) 5203–5213.

[14] K. Zhang, Q. He, J. H. Rao, Y. Wang, R. Zhang, X. Yuan, W. Feng, A. Huang, Correlation of textures and hemming performance of an AA6XXX aluminium alloy, Journal of Alloys and Compounds 853 (2021) 157081.

[15] O. Engler, V. Randle, Introduction to texture analysis: macrotexture, microtexture, and orientation mapping, second ed., CRC press, Taylor & Francis Group, 2009.

[16] I. Westermann, K. E. Snilsberg, Z. Sharifi, O. S. Hopperstad, K. Marthinsen, B. Holmedal, Three-point bending of heat-treatable aluminum alloys: influence of microstructure and texture on bendability and fracture behavior, Metallurgical and Materials Transactions A 42 (2011) 3386–3398.

[17] A. Saai, I. Westermann, S. Dumoulin, O. S. Hopperstad, Crystal plasticity finite element simulations of pure bending of aluminium alloy AA7108, International Journal of Material Forming 9 (2016) 457–469.

[18] A. Davidkov, M. Jain, R. Petrov, D. Wilkinson, R. Mishra, Strain localization and damage development during bending of Al–Mg alloy sheets, Materials Science and Engineering: A 550 (2012) 395–407.

[19] W. Muhammad, J. Kang, A. P. Brahme, U. Ali, J. Hirsch, H.-J. Brinkman, O. Engler, R. K. Mishra, K. Inal, Bendability enhancement of an age-hardenable aluminum alloy: Part I — relationship between microstructure, plastic deformation and fracture, Materials Science and Engineering: A 753 (2019) 179–191.

[20] W. Muhammad, A. P. Brahme, U. Ali, J. Hirsch, O. Engler, H. Aretz, J. Kang, R. K. Mishra, K. Inal, Bendability enhancement of an age-hardenable aluminum alloy: Part II — multiscale numerical modeling of shear banding and fracture, Materials Science and Engineering: A 754 (2019) 161–177.

[21] A. Pineau, A. A. Benzerga, T. Pardoen, Failure of metals I: Brittle and ductile fracture, Acta Materialia 107 (2016) 424 – 483.

[22] C. Tekoğlu, J. W. Hutchinson, T. Pardoen, On localization and void coalescence as a precursor to ductile fracture, Philosophical Transactions of the Royal Society A: Mathematical, Physical and Engineering Sciences 373 (2015) 20140121.

[23] B. H. Frodal, D. Morin, T. Børvik, O. S. Hopperstad, On the effect of plastic anisotropy, strength and work hardening on the tensile ductility of aluminium alloys, International Journal of Solids and Structures 188-189 (2020) 118 – 132.

[24] G. I. Taylor, Plastic strain in metals, J. Inst. Metals 62 (1938) 307–324.

[25] J. W. Hutchinson, Bounds and self-consistent estimates for creep of polycrystalline materials, Proceedings of the Royal Society of London A: Mathematical, Physical and Engineering Sciences 348 (1976) 101–127.

[26] U. F. Kocks, H. Chandra, Slip geometry in partially constrained deformation, Acta Metallurgica 30 (1982) 695 – 709.

[27] P. Van Houtte, On the equivalence of the relaxed taylor theory and the bishop-hill theory for partially constrained plastic deformation of crystals, Materials Science and Engineering 55 (1982) 69 – 77.

[28] F. Roters, P. Eisenlohr, L. Hantcherli, D. D. Tjahjanto, T. R. Bieler, D. Raabe, Overview of constitutive laws, kinematics, homogenization and multiscale methods in crystal plasticity finite-element modeling: Theory, experiments, applications, Acta Materialia 58 (2010) 1152–1211.

[29] A. K. Kanjarla, P. Van Houtte, L. Delannay, Assessment of plastic heterogeneity in grain interaction models using crystal plasticity finite element method, International Journal of Plasticity 26 (2010) 1220 – 1233.

[30] M. Knezevic, B. Drach, M. Ardeljan, I. J. Beyerlein, Three dimensional predictions of grain scale plasticity and grain boundaries using crystal plasticity finite element models, Computer Methods in Applied Mechanics and Engineering 277 (2014) 239–259.

[31] A. Eghtesad, K. Germaschewski, R. A. Lebensohn, M. Knezevic, A multi-GPU implementation of a full-field crystal plasticity solver for efficient modeling of high-resolution microstructures, Computer Physics Communications 254 (2020) 107231.

[32] W. G. Feather, H. Lim, M. Knezevic, A numerical study into element type and mesh resolution for crystal plasticity finite element modeling of explicit grain structures, Computational Mechanics 67 (2021) 33–55.

[33] W. Muhammad, U. Ali, A. P. Brahme, J. Kang, R. K. Mishra, K. Inal, Experimental analyses and numerical modeling of texture evolution and the development of surface roughness during bending of an extruded aluminum alloy using a multiscale modeling framework, International Journal of Plasticity 117 (2019) 93–121.

[34] M. B. Gorji, Instability and Fracture Models to Optimize the Metal Forming and Bending Crack Behavior of Al-Alloy Composites, Ph.D. thesis, ETH Zürich, 2015.

[35] M. B. Gorji, B. Berisha, P. Hora, F. Barlat, Modeling of localization and fracture phenomena in strain and stress space for sheet metal forming, International Journal of Material Forming 9 (2016) 573–584.

[36] M. B. Gorji, N. Manopulo, P. Hora, F. Barlat, Numerical investigation of the post-necking behavior of aluminum sheets in the presence of geometrical and material inhomogeneities, International Journal of Solids and Structures 102-103 (2016) 56–65.

[37] B. H. Frodal, S. Thomesen, T. Børvik, O. S. Hopperstad, On the coupling of damage and single crystal plasticity for ductile polycrystalline materials, International Journal of Plasticity 142 (2021) 102996.

[38] The Aluminium Association, International Alloy Designations and Chemical Composition Limits for Wrought Aluminum and Wrought Aluminum Alloys, 2015.

[39] F. Bachmann, R. Hielscher, H. Schaeben, Texture Analysis with MTEX – Free and Open Source Software Toolbox, Solid State Phenomena 160 (2010) 63–68.

[40] VDA, German Association of the Automotive Industry (VDA), VDA 238-100 Plate bending test for metallic materials, 2010.

[41] SCMM-hypo, SIMLab Crystal Mechnaics Model - hypoelastic formulation (SCMM-hypo) Version 3.0.0, 2022. URL: https://github.com/frodal/SCMM-hypo.

[42] X. Han, J. Besson, S. Forest, B. Tanguy, S. Bugat, A yield function for single crystals containing voids, International Journal of Solids and Structures 50 (2013) 2115 – 2131.

[43] J. Paux, L. Morin, R. Brenner, D. Kondo, An approximate yield criterion for porous single crystals, European Journal of Mechanics - A/Solids 51 (2015) 1 – 10.

[44] M. Khadyko, B. H. Frodal, O. S. Hopperstad, Finite element simulation of ductile fracture in polycrystalline materials using a regularized porous crystal plasticity model, International Journal of Fracture 228 (2021) 15–31.

[45] Texture2Abaqus, Version 1.0.0, 2022. URL: https://github.com/frodal/Texture2Abaqus.

[46] V. Tvergaard, Influence of voids on shear band instabilities under plane strain conditions, International Journal of Fracture 17 (1981) 389–407.

[47] A. L. Gurson, Continuum theory of ductile rupture by void nucleation and growth: Part I—Yield criteria and flow rules for porous ductile media, Journal of Engineering Materials and Technology 99 (1977) 2–15.

[48] T. F. Morgeneyer, M. Khadyko, A. Buljac, L. Helfen, F. Hild, A. Benallal, T. Børvik, O. S. Hopperstad, On crystallographic aspects of heterogeneous plastic flow during ductile tearing: 3D measurements and crystal plasticity simulations for AA7075-T651, International Journal of Plasticity 144 (2021) 103028.

[49] J. M. Dowling, J. W. Martin, The influence of MN additions on the deformation behaviour of an Al-Mg-Si alloy, Acta Metallurgica 24 (1976) 1147 – 1153.

[50] T. F. Morgeneyer, M. J. Starink, S. C. Wang, I. Sinclair, Quench sensitivity of toughness in an Al alloy: Direct observation and analysis of failure initiation at the precipitate-free zone, Acta Materialia 56 (2008) 2872 – 2884.

[51] E. Christiansen, C. D. Marioara, K. Marthinsen, O. S. Hopperstad, R. Holmestad, Lattice rotations in precipitate free zones in an Al-Mg-Si alloy, Materials Characterization 144 (2018) 522 – 531.